

Research Article pubs.acs.org/acscatalysis

# Elucidating the Structure of Bimetallic NiW/SiO<sub>2</sub> Catalysts and Its Consequences on Selective Deoxygenation of m-Cresol to Toluene

Feifei Yang, Mallikharjuna Rao Komarneni, Nicole J. Libretto, Liwen Li, Wei Zhou, Jeffrey T. Miller, Qingfeng Ge, Xinli Zhu,\* and Daniel E. Resasco\*



Cite This: ACS Catal. 2021, 11, 2935-2948



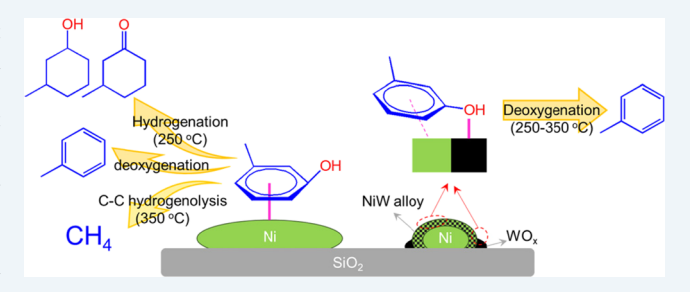
**ACCESS** 

Metrics & More

Article Recommendations

Supporting Information

ABSTRACT: As a non-noble metal, Ni could offer significant economic advantages if used as a catalyst for hydrodeoxygenation (HDO) of lignin-derived phenolics to produce aromatics. However, on unmodified Ni catalysts, the desirable direct deoxygenation reaction must compete with high rates of phenylring hydrogenation and C-C hydrogenolysis reactions, which lead to low aromatics yields. Here, we report on a bimetallic NiW/SiO<sub>2</sub> (W/Ni = 1) prepared by coimpregnation that shows an HDO reaction rate of *m*-cresol almost an order of magnitude higher than that on Ni/SiO<sub>2</sub> at 350 °C and 1 atm H<sub>2</sub>. More importantly, under



these conditions, this catalyst exhibits a complete inhibition of CH<sub>4</sub> formation, while at a temperature as low as 250 °C, the dominant product is still toluene, with minimal formation of ring-saturation products. To elucidate the structure of this catalyst, a detailed characterization was performed by combination of several techniques. It was found that the calcined NiW/SiO<sub>2</sub> exhibits a large extent of Ni-W oxide interaction. After reduction at 500 °C, a thin NiW alloy shell with a small Ni core and WO<sub>x</sub> in close proximity are formed, with a strong interaction between Ni and adjacent W species. The electronic modifications of Ni and W species were monitored by X-ray photoelectron spectroscopy and it was found that these interactions alter the surface properties of the alloy, resulting in significantly weakened CO chemisorption. This unique structure provides a balanced hydrogenation, oxophilicity, and C-O cleavage activity, which result in a significantly improved rate and selectivity toward toluene with inhibition of CH<sub>4</sub> and hydrogenation product formation.

KEYWORDS: hydrodeoxygenation, m-cresol, nickel, NiW/SiO2 bimetallic catalyst, C-C hydrogenolysis

### 1. INTRODUCTION

Fast pyrolysis of biomass lignin produces bio-oil, rich in phenolic compounds. Its high oxygen content makes the crude bio-oil incompatible with today's infrastructure of hydrocarbon fuels. 1-3 Therefore, catalytic hydrodeoxygenation (HDO) is a key step to upgrade bio-oil to fuels and chemicals. The need to develop low-cost, active, selective, and stable HDO catalysts has inspired numerous studies.<sup>4–7</sup> In some cases, HDO has been carried out in the liquid phase at relatively low temperatures and high H<sub>2</sub> pressure to simulate the treatment of condensed bio-oil liquids. Under these conditions, the HDO catalysts normally contain a hydrogenating metal and an acid function, which enable hydrogenation and dehydration reactions, respectively. As a result, the HDO reaction follows the hydrogenation-dehydration (HYD) mechanism, producing saturated cyclohexanes as the final product.<sup>8-11</sup> Alternatively, the HDO reaction can be performed in the vapor phase at relatively high temperatures and low H2 pressure, to simulate the direct treatment of pyrolysis vapor before condensation. Under these conditions, aromatics are found to be the dominant products. 12-16 Selective direct deoxygenation (DDO) of phenolics to aromatics is attractive since it consumes much lower amounts of valuable H2 than the other processes.

Many efforts have been made to understand the DDO mechanism and develop selective catalysts for this reaction. Although typical noble-metal hydrogenating catalysts, such as Pt and Pd, are able to catalyze the DDO reaction to aromatics, they are more active for hydrogenation, particularly at low temperatures.<sup>17</sup> Theoretical calculations indicate that phenol adsorption on the hydrogenating metal surface through its phenyl ring instead of O due to the low oxophilicity results in a higher preference for phenyl-ring hydrogenation over C-O cleavage. 18 Other studies have shown that the combination of a hydrogenating metal with an oxophilic metal or metal oxide is an effective approach to improve the selective deoxygenation of phenolics to aromatics, since these bifunctional catalysts

Received: December 18, 2020 Revised: February 3, 2021 Published: February 18, 2021





ACS Catalysis pubs.acs.org/acscatalysis Research Article

enable both hydrogenation and O adsorption as well as C–O cleavage capabilities. Since non-noble metal-based catalysts appear economically more desirable than noble metals, a broad interest has arisen in designing this type of catalysts for deoxygenation of phenolics. 5

Among them, Ni is economically attractive; however, it suffers from a high tendency for C–C cleavage reactions that form CH<sub>4</sub>, especially at high reaction temperatures, which are usually needed for deoxygenation. Therefore, the competition between C–C hydrogenolysis and deoxygenation makes designing Ni-based catalysts a great challenge. Modifying the Ni catalyst by oxophilic promoters can promote selective deoxygenation of phenolics.<sup>19</sup> For instance, the Fe-, Re-, Ga-, and Co-modified Ni catalysts enhance deoxygenation; however, they usually display residual C–C hydrogenolysis activity, at a relatively large extent.<sup>22–24,29</sup>

Recently, WO<sub>x</sub>-modified hydrogenating metal (Pt, Pd, Ru, and Ni) catalysts have been reported to be efficient for HDO of phenolics. 30-38 Wang et al. prepared a Pt-WO<sub>x</sub>/C catalyst by a sequential impregnation method in which Pt is deposited first; this catalyst showed toluene selectivity >94% during HDO of m-cresol at 573 K and 36 bar H<sub>2</sub>. They proposed that the active deoxygenation site is the oxygen vacancy (or redox) sites provided by WO<sub>x</sub> species, while the role of Pt was to stabilize a WO<sub>x</sub> film by facilitating the formation of oxygen vacancy.<sup>30</sup> In another study, Hong et al. prepared a Pd-WO<sub>x</sub>/ γ-Al<sub>2</sub>O<sub>3</sub> catalyst by impregnation of Pd with preprepared  $WO_x/\gamma$ -Al<sub>2</sub>O<sub>3</sub> and tested it for guaiacol HDO at 200-300 °C and 7 MPa H<sub>2</sub>. They suggested that the preformed monolayer of WO<sub>x</sub> on γ-Al<sub>2</sub>O<sub>3</sub> plays an essential role in dehydration of phenyl-ring-hydrogenated guaiacol intermediates during HDO, due to its high acid density.<sup>31</sup> Meng et al. reported that the RuW alloy formed from reduction at 800 °C of coimpregnation-prepared RuW/SiO2 is active for hydrogenolysis of aromatic ethers to arenes at 175 °C and 1 MPa H<sub>2</sub>. Whereas, other studies suggested that Ru-WO<sub>x</sub> is the active site for HDO of phenolics or phenyl ethers to aromatics in which the strong acid site formed from interactions of WO, with the support (SiAl or ZrO<sub>2</sub>) plays a role in the overall reaction and selectivity.33-30

Since sulfided NiW catalysts are typical industrial hydrodesulfurization catalysts, NiW-based catalysts have also been explored in several phenolic HDO studies under various reaction conditions. <sup>37-39</sup> For example, Hsu et al. prepared the NiW/SiO<sub>2</sub> catalyst by a coimpregnation method, calcined at 400 °C and reduced at 800 °C, leading to the formation of metallic Ni and W phases.<sup>37</sup> Both HYD and DDO paths were identified during HDO of p-cresol at 250 °C and 1 MPa H<sub>2</sub>, and the Ni-WO<sub>x</sub> neighbor is suggested to be the active site for DDO. Likewise, Echeandia et al. prepared a NiW/AC catalyst by a sequential impregnation method; after calcination and reduction at 400 °C, it was tested for HDO of phenol at 423-573 K and 1.5 MPa H<sub>2</sub>. <sup>38</sup> Under these reduction conditions, the catalyst was only partially reduced, so the authors suggested that the activation of the oxy-group in phenol occurs at the oxide WOx sites. It must be noted that these previous works were performed under high H2 pressures, which led to the formation of significant amounts of phenylring-saturation products, in addition to aromatics. Furthermore, the wide range of catalyst preparation and activation procedures, as well as reaction conditions, make the detailed structure of these NiW catalysts and those of noble metal-W catalysts and their consequences on HDO activity unclear.

Therefore, the present work aims at the investigation of the NiW fine structure and its consequences in HDO. We selected simple *m*-cresol as a phenolic model compound to focus on the effect of the catalyst structure on the performance of C<sub>aromatic</sub>-OH breakage avoiding the influence of other functional groups, such as the methoxy group. In addition, cresol is also an important intermediate product during conversion of complex phenolics, such as guaiacol. 40-42 We have varied the preparation procedure of the NiW/SiO<sub>2</sub> catalyst, tested for HDO of m-cresol at 250-350 °C and 1 atm H<sub>2</sub>, performed detailed characterization using several techniques and correlated the fine structure of the NiW catalysts with the catalytic performance. The strong interaction between Ni and W oxides results in a Ni core and NiW alloy shell with WO<sub>x</sub> in close proximity after reduction at 500 °C, which shows an order of magnitude higher activity than the pure Ni site in Ni/SiO<sub>2</sub>. More importantly, the undesirable side reaction of C-C hydrogenolysis is avoided and ring hydrogenation is inhibited to a large extent.

# 2. EXPERIMENTAL SECTION

**2.1. Catalyst Preparation.** The catalysts were prepared by an incipient wetness impregnation method. Briefly, aqueous solutions of calculated amounts of Ni(NO<sub>3</sub>)<sub>2</sub> 6H<sub>2</sub>O (Aldrich) and/or (NH<sub>3</sub>)<sub>6</sub>(H<sub>2</sub>W<sub>12</sub>O<sub>40</sub>) nH<sub>2</sub>O (Aldrich) were added dropwise onto the SiO<sub>2</sub> support (Sigma). In all samples, the Ni loading was kept constant at 5 wt %, while the W loading was varied from 0 to 31.3 wt % to obtain W/Ni molar ratios varying from 0 to 2. A monometallic W/SiO<sub>2</sub> with a W loading of 15.7 wt % was prepared accordingly. The bimetallic NiW catalysts prepared by the coimpregnation method were identified as NiWXY, where XY represents the molar ratio of Ni:W. For example, the NiW11 sample indicates that the Ni:W molar ratio is 1:1, with Ni and W loadings of 5 and 15.7 wt %, respectively. After impregnation, the catalysts were dried in an oven at 120 °C for 12 h and then calcined at 500 °C for 4 h.

To test the influence of the preparation procedure, equimolar Ni:W (1:1) catalysts were also prepared by sequential impregnation and were named Ni $^{\rm I}W^2-11$  or W $^{\rm I}Ni^2-11$ , depending on whether Ni or W was loaded first. To evaluate the effect of calcination temperature, the NiW11 sample was calcined at varying temperatures in the 450–750  $^{\circ}$ C range. These catalysts were labeled with the calcination temperature. That is, NiW11–750 represents the NiW11 catalyst calcined at 750  $^{\circ}$ C.

**2.2. Catalyst Characterization.**  $N_2$  adsorption—desorption isotherms were recorded in an automatic Micrometrics Digisorb 2600 analyzer. X-ray diffraction patterns were collected on an XRD Rigaku D/max 2500 diffractometer with a  $Cu(K\alpha)$  radiation source. The Raman spectra were measured on a Renishaw Raman spectrometer, using an  $Ar^+$  ion laser (532 nm) as the exciting light source. Diffuse-reflectance ultraviolet visible (DR UV—vis) spectra were acquired on a UV-2550 spectrophotometer. Infrared spectra of pyridine adsorption were recorded in a Frontier spectrometer (PerkinElmer).

 $\rm H_2$  temperature-programmed reduction ( $\rm H_2\text{-}TPR$ ) was performed on a Chemisorb 2750 (Micrometrics). In each measurement, a 40 mg sample was placed in a U-tube quartz reactor and pretreated at 300 °C for 1 h and cooled down to room temperature in flowing  $\rm N_2$  gas, which was then switched to 5%  $\rm H_2/Ar$ . Once the background was stabilized, the sample

was heated to 800  $^{\circ}$ C at a heating rate of 10  $^{\circ}$ C/min. The  $H_2$  uptake was monitored on a thermal conductivity detector.

In situ X-ray absorption spectroscopy (XAS) experiments were performed at the 10-BM beamline at the Advanced Photon Source (APS) at Argonne National Laboratory. Measurements were performed at the Ni K (8.333 keV) and W L3 (10.207 keV) edges for each sample. Samples were pressed into a stainless-steel sample holder and placed in a quartz tube sample cell. The cell was sealed and treated at 500 °C in 3.5% H<sub>2</sub>, cooled to room temperature in He, and then transferred to the beamline. The He tank was connected to a gas purifier to reduce the possibility of O2 exposure. After H2 treatment at each temperature, the sample cell was purged with 20% O<sub>2</sub> at room temperature for 15 min to allow for surface oxidation of the nanoparticles, and a second spectrum was recorded. The measurements were performed in transmission mode in fast scan mode from 250 eV below the edge to 800 eV above the edge; it took approximately 10 min per scan, ranging 8132-9000 and 9957-11,007 eV for the Ni and W edges, respectively. The data were fitted using WinXAS 3.1 software to determine the coordination number (CN) and bond distance (R) using standard procedures.

The transmission electron microscopy (TEM) images were obtained on a JEM 2010F field emission system. X-ray photoelectron spectroscopy (XPS) was performed on a PHI 5800 ESCA system, equipped with an Al K $\alpha$  X-ray anode. All spectra were referenced to C 1 s at a binding energy (BE) of 284.8 eV.

CO chemisorption and NH $_3$  temperature-programmed desorption (NH $_3$ -TPD) were measured in a microreactor equipped with a Cirrus 200 mass spectrometer. For each run, a 100 mg sample was loaded in the microreactor, reduced in situ at 500 °C for 1 h in flowing H $_2$ , and purged with He for 0.5 h. CO chemisorption was conducted at room temperature, by sending pulses of 5% CO/He over the sample until a constant CO peak was obtained. For NH $_3$ -TPD, the temperature was cooled to 50 °C. First, the pretreated sample was exposed to flowing 2% NH $_3$ /He gas for 0.5 h and purged with flowing He for another 0.5 h to remove physically adsorbed NH $_3$ . Finally, the TPD ramp was started, heating the sample at a rate of 10 °C/min up to 800 °C.

Density functional theory (DFT) calculations for O and H adsorption were performed using the Vienna Ab initio Simulation Package (VASP). 43,44 Projector augmented wave (PAW) potentials 45 were used to represent the effective cores. The Perdew-Burke-Ernzerhof (PBE) functional was used to calculate exchange and correlation energy. 46 The cutoff energy of the plane-wave basis set was 400 eV. For bulk Ni, Re, Mo, and W, a Monkhorst-Pack grid of 6 × 6 × 6 was used, and the interatomic forces were minimized to 0.02 eV/Å for structural relaxations. A three-layer slab with a  $(2 \times 2)$  surface unit cell constructed from the relaxed bulk was used to represent different metal surfaces. The most stable surfaces of (111), (0001), (110), and (110) were used to represent Ni, Re, Mo, and W, respectively. A vacuum space of 10 Å along the zdirection was used to avoid direct interactions between the periodic images of the slab. The bottom two layers of atoms were fixed, while the atoms on the top layer and adsorbate were fully optimized. The adsorption energy was referenced to the bare slab and 1/2 H<sub>2</sub> or O<sub>2</sub>.

**2.3. Catalytic Evaluation.** The vapor phase conversion of *m*-cresol was conducted in a fixed-bed flow reactor at atmospheric pressure. The catalyst (40–60 mesh) was loaded

between two layers of quartz wool on the top of the thermocouple in a steel tube reactor (6 mm diameter). Before each run, the catalyst was reduced at 400–600 °C for 1 h in H<sub>2</sub> and then cooled down to the reaction temperature (250–350 °C). *m*-Cresol was fed by a syringe pump (KDS100, kd scientific) and vaporized at 180 °C before entering the reactor. The products were analyzed and quantified by online gas chromatography (GC, HP 5890). To fully identify the products, the effluent was trapped in ethanol and analyzed by GC-mass spectrometry (MS) (Shimadzu QP2010S). Fresh samples were used in each reaction. The space time (W/F, h) is defined as the ratio of the weight of the catalyst (g) to organic feed flow rate (g/h), which represents the residence time of the organic feed going through the catalyst bed. The conversion and yield are reported in mol<sub>carbon</sub> %.

#### 3. RESULTS AND DISCUSSION

3.1. Catalytic Performance. 3.1.1. Effects of Calcination and Reduction Temperature. The structure of NiW catalysts and consequently their catalytic performance can be significantly influenced by the preparation procedure. Therefore, calcination and reduction temperatures were first optimized on the equimolar NiW11 sample. First, the sample was tested for HDO of m-cresol at 350 °C with a W/F of 0.05 h after calcining at varying temperatures, while keeping the reduction temperature at 500 °C. As shown in Figure S1A, the m-cresol conversion and toluene (Tol) yield increased with increasing calcination temperature from 400 to 500  $^{\circ}\text{C}$  but remained constant beyond this temperature, at least up to 750 °C. Likewise, the NiW11 sample precalcined at 500 °C was tested after varying the reduction temperature in the range 400-600 °C. As shown in Figure S1B, both the *m*-cresol conversion and Tol yield showed a maximum after reduction temperatures of 500-550 °C but decreased beyond this temperature. Thus, calcination at 500 °C followed by reduction at 500 °C appeared to be the optimal pretreatment for HDO, which were selected for testing all the other preparation parameters.

3.1.2. Effect of Ni and W Loading Sequence. It has been previously observed that the extent of Ni-W interaction and surface composition of exposed species of NiW catalysts can be strongly influenced by the sequence of loading Ni and W onto the support. 30,31,37,38 Here, the HDO of *m*-cresol was compared on three different 5 wt % Ni-15.66 wt % W/SiO<sub>2</sub> (W/Ni molar ratio of 1) samples prepared by coimpregnation (NiW11) and sequential impregnation (Ni<sup>1</sup>W<sup>2</sup>-11 and W<sup>1</sup>Ni<sup>2</sup>-11). As shown in Table 1, although Tol was the major product on all samples, NiW11 showed five and three times higher m-cresol conversion than Ni<sup>1</sup>W<sup>2</sup>-11 and W<sup>1</sup>Ni<sup>2</sup>-11, respectively. Apparently, coimpregnation results in an optimal structure for efficient HDO. In addition, the higher mcresol conversion observed on W1Ni2-11 compared to Ni<sup>1</sup>W<sup>2</sup>-11 suggests that the presence of Ni on the surface is an important requirement for high HDO activity. From this analysis, the coimpregnation method was selected for further optimization of the NiW catalysts.

**3.1.3. Effect of W/Ni Molar Ratio.** A series of NiW catalysts with 5 wt % Ni and varying W/Ni ratios were tested in the HDO of *m*-cresol at 350 °C. As shown in Figure 1A, the intrinsic rates of *m*-cresol conversion and Tol formation increased almost linearly with the W/Ni ratio from 1.89 and 0.41  $\mu$ mol  $g_{cat}^{-1}$  s<sup>-1</sup> on Ni/SiO<sub>2</sub> (W/Ni = 0) to 17.54 and 16.30  $\mu$ mol  $g_{cat}^{-1}$  s<sup>-1</sup> on NiW11 (W/Ni = 1), respectively.

Table 1. Effect of Ni and W Loading Sequence of  $NiW/SiO_2$  for HDO of m-Cresol<sup>a</sup>

catalyst	$Ni^1W^2-11$	NiW11	$W^1Ni^2-11$
conversion (%) product yield (%)	6.2	34.2	11.2
Tol	4.4	31.7	8.6
DMB	0.1	0.8	0.1
p/o-cresol	1.0	0.9	1.0
xylenol	0.1	0.3	0.1
Ph	0.4	0.1	0.8
LH	0.3	0.4	0.6

<sup>a</sup>Reaction conditions: T = 350 °C; TOS = 20 min; W/F = 0.05 h. Tol = toluene, DMB = dimethyl biphenyl, Ph = phenol, LH = light hydrocarbon with carbon number between 2 to 6.

That is, the overall reaction rate and deoxygenation rate on Ni/SiO<sub>2</sub> were improved by ~9 and ~40 times on NiW11, respectively. This result highlights the crucial role that W plays in improving the HDO activity of the Ni catalyst. However, further increase in the W/Ni ratio from 1 to 2 resulted in an almost negligible increase in both m-cresol conversion and Tol formation rates. Moreover, the Ni-free sample, W/SiO<sub>2</sub>, showed no deoxygenation activity under identical reaction conditions. These results indicate that both Ni and W are essential for deoxygenation, but the presence of W greatly enhances its activity. The Arrhenius plots for the Tol formation on NiW21, NiW11, and NiW12, as well as Ni<sup>1</sup>W<sup>2</sup>-11 and W<sup>1</sup>Ni2-11 catalysts at 275-350 °C are summarized in Figure 1B. Interestingly, while these catalysts show very different HDO activity, the apparent activation energies for Tol formation are very similar (48.7-59.2 kJ/mol). This trend would indicate that the samples have a different density of active sites of the same nature.

The variation of product distribution with space time (W/F) on the NiW11 sample can be compared at different temperatures to the behavior exhibited by a conventional Ni/SiO<sub>2</sub> catalyst. As reported in previous work (see Figure S2 and Tables S1 and S2), <sup>28</sup> monometallic Ni/SiO<sub>2</sub> favors C–C hydrogenolysis at 350 °C and atmospheric pressure, producing CH<sub>4</sub> as the dominant product (100% selectivity) at conversion >90%; while it preferentially catalyzes phenyl-ring hydrogenation at 250 °C, producing methylcyclohexanone (MCHone) and methylcyclohexanol (MCHol) as the major

products (selectivity >70%) at conversions <20%. By contrast, the addition of W to Ni/SiO<sub>2</sub> significantly changes the product distributions. As shown in Figure 2A and Table S1, at 350 °C, the NiW11 sample produced mostly Tol as the deoxygenation product with only a low production of dimethyl biphenyl (DMB), as the secondary product. Interestingly, no CH<sub>4</sub> was obtained from hydrogenolysis. Similarly, at 250 °C (Figure 1B and Table S2), Tol was also the primary and major product, with methylcyclohexane (MCHane) being a minor secondary product. Feeding MCHol as the reactant indicated that MCHane is formed from secondary dehydration of MCHol obtained by hydrogenation of the ring (Figure S3), which shows that ring hydrogenation on Ni is strongly inhibited by the addition of W. In summary, it is clear that the presence of W promotes deoxygenation toward Tol, while inhibiting C-C hydrogenolysis at 350 °C and phenyl-ring hydrogenation at 250 °C, the two dominant paths on the unmodified Ni surface.

**3.2. Catalyst Characterization.** To unveil the structure of the NiW bimetallic catalysts and the influence of such structure on the HDO pathway, a detailed characterization was performed by combining several techniques. The amount of metal loading and the specific surface area ( $S_{\rm BET}$ ) are shown in Table 2. As expected, the surface area decreased with increasing metal loadings.

XRD patterns of NiW catalysts calcined at 500 °C are shown in Figure 3A. Monometallic Ni/SiO<sub>2</sub> shows diffractions corresponding to FCC NiO, while W/SiO2 presented diffractions of orthorhombic WO3. Increasing the W loading in the bimetallic NiW catalysts caused the NiO diffraction peaks to broaden and weaken, and even disappeared for the NiW11 sample as well as for those samples with higher W loadings. The particle size estimated from the broadening of the NiO (101) peak at 37.26° decreased from 21.0 nm for Ni/ SiO<sub>2</sub> to 13.8 nm for the bimetallic NiW21; moreover, it became undetectable due to a very high dispersion for NiW11, which is also confirmed by other characterizations (see below). At the same time, the presence of Ni changed the resulting structure of WO3, which was found to be only orthorhombic on the monometallic W/SiO<sub>2</sub> to a mixture of both orthorhombic and low-crystallinity WO<sub>3</sub><sup>47</sup> for NiW12, and only low-crystallinity WO3 for NiW11 and NiW21. A similar analysis on the peak at  $2\theta = 24.21-24.51^{\circ}$  yielded estimated particle sizes for WO<sub>3</sub> of 5.2, 6.2, 13.2, and 13.5 nm for the NiW21, NiW11, NiW12, and W/SiO<sub>2</sub> samples, respectively

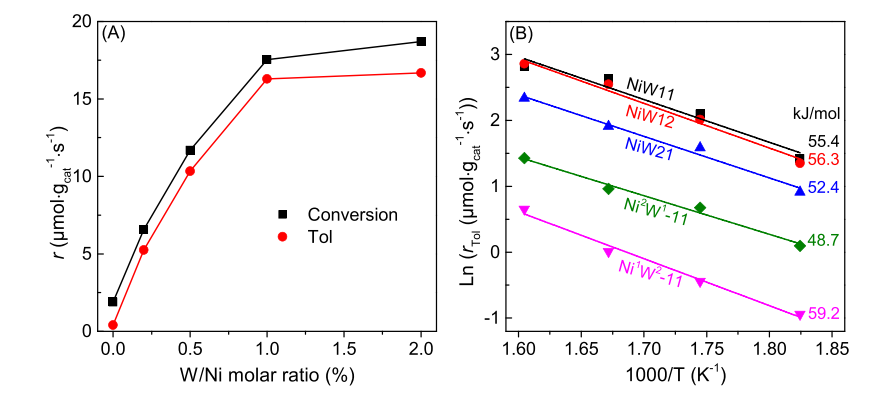
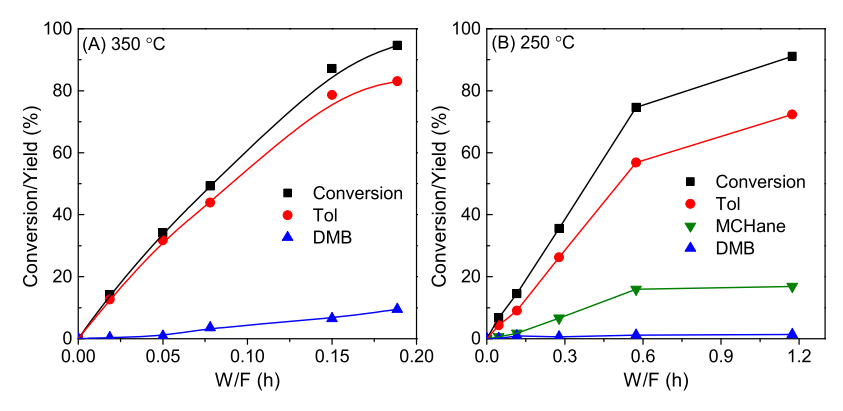


Figure 1. (A) Effect of the W/Ni molar ratio of NiW/SiO<sub>2</sub> catalysts with 5 wt % Ni while varying W loadings on the intrinsic reaction rates of m-cresol conversion and Tol formation at 350 °C. (B) Arrhenius plots of m-cresol deoxygenation to Tol on different catalysts at 275–350 °C. Reaction conditions: P = 1 atm, TOS = 20 min, conversion was kept under 10% by adjusting the W/F. The inset number shows the apparent activation energy for Tol formation on each catalyst with a unit of kJ/mol.



**Figure 2.** *m*-Cresol conversion and product distributions as a function of W/F over NiW11 at different temperatures: (A) T = 350 °C; (B) T = 250 °C. Reaction conditions: P = 1 atm, H<sub>2</sub>/m-cresol = 60, and TOS = 20 min.

Table 2. W/Ni Molar Ratio, Ni and W Loadings, Specific Surface Area from BET, and Acid Density for Different Catalysts

	W/Ni	loadings (wt %)		loadings (wt %)		$S_{\text{BET}}$	acid density <sup>a</sup>
catalyst	molar ratio	Ni	W	m <sup>2</sup> /g	$\mu$ mol/ $g_{cat}$		
Ni/SiO <sub>2</sub>		5.0		181	15.2		
NiW51	0.2	5.0	3.13	176	43.4		
NiW21	0.5	5.0	7.83	169	84.1		
NiW11	1	5.0	15.66	152	134.8		
NiW12	2	5.0	31.32	109	190.6		
$W/SiO_2$			15.66	181	164.4		
a 11	ATT TIPE						

<sup>a</sup>measured by NH<sub>3</sub>-TPD.

(Table S3). In addition, XPS results also confirmed that the W species in these samples have a valence state of 6+ (Figure S4). These results indicate that the strong interaction between NiO and WO $_3$  facilitates the dispersion of both oxides, and changes orthorhombic WO $_3$  into a low-crystallinity WO $_3$  due to its interaction with NiO. <sup>47</sup> Interestingly, no NiWO $_4$  was found in any of these samples.

Raman spectroscopy was employed to characterize the interactions between NiO and WO<sub>3</sub> species in the calcined samples. As shown in Figure 4, the Ni/SiO<sub>2</sub> sample shows a weak and broad Ni–O vibration band, centered at 550 cm<sup>-1</sup>. In turn, the W/SiO<sub>2</sub> sample shows two intense bands at 715 and 807 cm<sup>-1</sup>, which are attributed to O–W–O vibrations in crystalline WO<sub>3</sub> particles. Increasing W loadings in the samples from NiW51 to NiW11 resulted in the appearances of

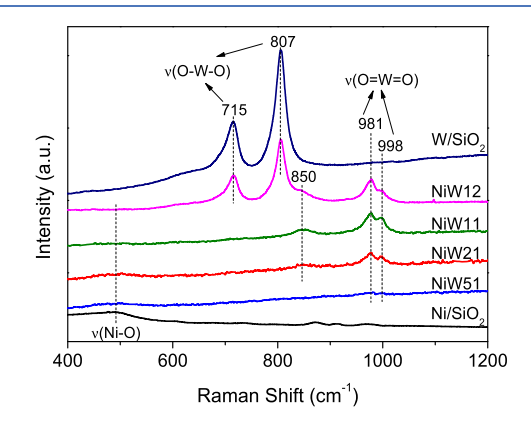


Figure 4. Raman spectra of different catalysts after calcination at 500  $^{\circ}\text{C}.$ 

two bands at 981 and 998 cm<sup>-1</sup>, as well as a weak band at 850 cm<sup>-1</sup>. The former two bands can be ascribed to asymmetric and symmetric vibrations of O=W=O in a structure of  $(Si-O)_2-W(=O)_2$  or  $(Ni-O)_2-W(=O)_2$ , respectively. Since  $W/SiO_2$  did not show such O=W=O vibration bands, these bands are likely related to the structure of  $(Ni-O)_2-W(=O)_2$ , suggesting a strong interaction between Ni and W oxides. Analogous to Zr-O-Mo stretching bands previously observed on  $ZrO_2$ -supported  $MoO_3$ , the latter band is likely related to the W-O-Ni stretching. These results indicate that the interaction between Ni and W oxides is very significant on the calcined NiW11 sample. This interaction is responsible for a high dispersion of  $WO_3$ . Further increasing the W loading to

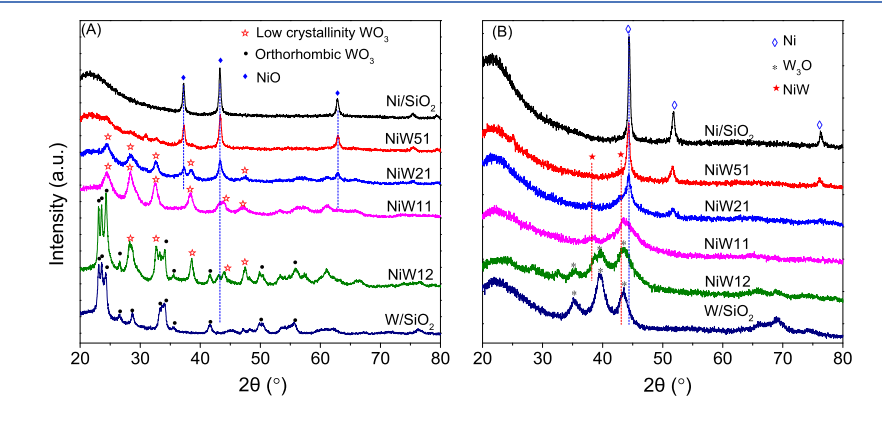
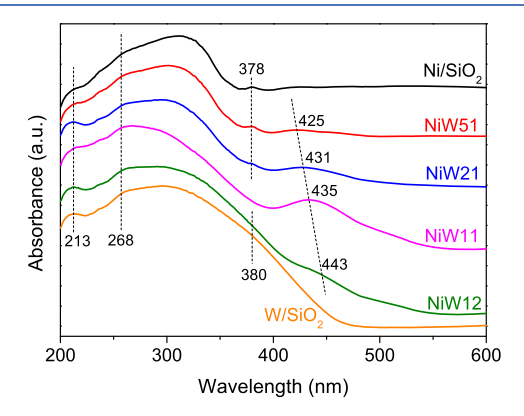


Figure 3. XRD patterns of different catalysts after calcination at 500  $^{\circ}$ C (A) and after reduction at 500  $^{\circ}$ C (B). Low-crystallinity WO<sub>3</sub> could also be nanoparticles of undoped and NiO-doped WO<sub>3</sub>.

the NiW12 sample led to the appearance of intense bands at 715 and 807 cm<sup>-1</sup>, ascribed to crystalline WO<sub>3</sub> nanoparticles as excess W species, without a direct interaction with Ni.

UV-vis spectroscopy was used to further investigate the structure of the metal oxides on the calcined samples. As shown in Figure 5, Ni/SiO<sub>2</sub> showed an intense band at 313 nm



**Figure 5.** UV-vis spectra of different catalysts after calcination at 500 °C.

and a weak band at 378 nm, which are related to NiO nanoparticles.<sup>52,53</sup> These bands were weakened and disappeared with increasing W loadings to NiW11 and NiW12 samples, which might be hidden in the bands of WO<sub>3</sub>. The absorption bands at 213 and 268 nm are stronger for the Wcontaining catalysts, which could be attributed to isolated WO<sub>4</sub> tetrahedral species and partially polymerized W species in octahedral coordination, respectively, as previously proposed. 50 The presence of an adsorption band centered at 380 nm and extended to 450 nm for W/SiO<sub>2</sub> indicates the presence of WO<sub>3</sub> nanoparticles, in agreement with XRD and previous observation.<sup>54</sup> This band weakened with an increasing Ni/W ratio, suggesting that the content of isolated WO3 nanoparticles decreases with the presence of Ni. In addition, a weak band at 425 nm was observed for the NiW51 sample. The band was red-shifted with increasing W content, and its intensity was maximized for the NiW11 sample. This shift points to a reduced energy band gap for both oxides, 55,56 reflecting the strong interaction between W and Ni oxides. In summary, XRD, Raman, and UV-vis characterization results give consistent evidence for a strong interaction of Ni and W oxides in the calcined samples, with this interaction maximized in the equimolar NiW11 sample.

H<sub>2</sub>-TPR not only allows for an additional characterization of the samples in the oxidic form but also provides a description of the reduction process occurring on the different samples. As shown in Figure 6, while Ni/SiO<sub>2</sub> shows a rather sharp H<sub>2</sub> consumption peak, centered at 337 °C, W/SiO<sub>2</sub> starts its reduction at much higher temperatures, with a maximum at about 775 °C. The H<sub>2</sub> consumption peaks for the bimetallic NiW catalysts lies between those for Ni/SiO<sub>2</sub> and W/SiO<sub>2</sub> and increased to higher temperatures with increasing W. This trend gives further evidence for the large extent of interaction between Ni and W oxides, which facilitates the reduction of W oxide, but in turn retards that of NiO. Quantification of these results indicate that the molar ratio of H2 consumption to Ni (H<sub>2</sub>/Ni) for the Ni/SiO<sub>2</sub> sample was 0.99, indicating the complete reduction of NiO to metallic Ni. The H<sub>2</sub>/W ratio for W/SiO<sub>2</sub> was 2.7, in agreement with previous work, <sup>57</sup> indicating

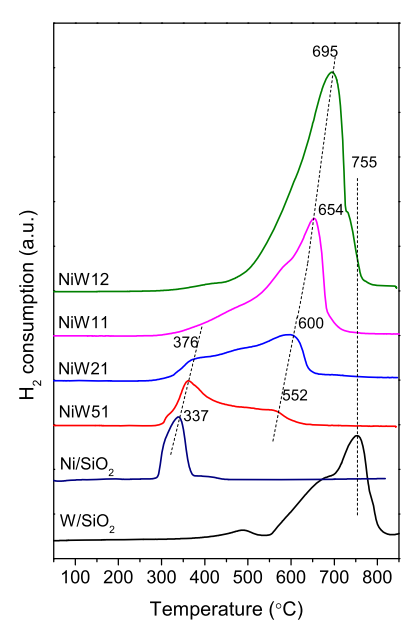


**Figure 6.**  $H_2$ -TPR profiles of different catalysts after calcination at 500  $^{\circ}C$ 

an incomplete reduction of W since complete reduction of  $WO_3$  to metallic W would result in a  $H_2/W$  ratio of 3. After subtracting the  $H_2$  consumed by complete reduction of NiO, the  $H_2/W$  ratios were below 3.0 for all the NiW bimetallic catalysts except for NiW51, suggesting that the W species cannot be completely reduced even in the presence of Ni. Note that the major reduction peaks of NiW catalysts are at higher temperatures than those reported for bimetallic NiMo, NiRe, and NiFe catalysts (at <500 °C) with similar molar compositions. This comparison suggests a stronger interaction between Ni and W in the oxidized states than with the other transition metals since the reduction of NiW occurs at a relatively low rate. In turn, this enhanced interaction may result in a higher dispersion of the surface species.

After reduction at 500 °C for 1 h, the NiW catalysts were characterized by XRD. As shown in Figure 3B, the monometallic Ni/SiO<sub>2</sub> shows diffractions at  $2\theta = 44.51$ , 51.85, and 76.37°, attributed, respectively, to the (111), (200), and (220) FCC planes of metallic Ni. Likewise, the W/SiO<sub>2</sub> sample displayed diffractions at  $2\theta = 35.31$ , 39.76, and  $43.76^{\circ}$ corresponding to (002), (012), and (112) planes of W<sub>3</sub>O. Increasing the W/Ni ratio in bimetallic NiW catalysts in the range of W:Ni ratio = 0-1 resulted in weaker and broader Ni diffractions. The Ni particle sizes estimated from these peaks are 19.9, 12.7, and 5.6 nm for Ni/SiO<sub>2</sub>, NiW51, and NiW21, respectively. The large Ni particle size of Ni/SiO2 is one of the reasons for its low HDO activity. <sup>13,58</sup> For a W:Ni ratio  $\geq 1$ , the Ni diffractions disappeared which indicates that Ni became very highly dispersed; at the same time, the NiW alloy ( $2\theta =$ 42.99 and 38.96°) and W<sub>3</sub>O ( $2\theta = 35.31$ , 39.76, and 43.76°) diffractions emerged on these samples and they became more intense with increasing W. The estimated NiW alloy particle sizes (based on the peak at 38.96°) are 4.2 and 6.5 nm for the NiW11 and NiW12 samples, while the W3O particle (at 39.76°) sizes are 2.3 and 4.9 nm for the NiW12 and W/SiO<sub>2</sub> samples, respectively. The formation of the NiW alloy has also been reported on bimetallic catalysts under similar pretreatment conditions.<sup>59</sup> It is evident that in addition to the ACS Catalysis pubs.acs.org/acscatalysis Research Article

formation of the NiW alloy, the interactions between Ni and W oxides make both Ni and  $W_3O$  particles smaller.

An apparent contradiction is that the H<sub>2</sub>-TPR shows that only a minor fraction of NiW11 gets reduced below 500 °C (Figure 6) while XRD of the sample reduced at this temperature shows a deep reduction with formation of Ni, W<sub>3</sub>O, and NiW alloys (Figure 3B). The reason for this difference is that the reduction conditions are substantially different. That is, in the TPR, the sample is continuously changing during the heating ramp, while in the reduction pretreatment, the sample remains at 500 °C for 1 h. Also, the partial pressure of H<sub>2</sub> in the TPR is much lower than that of pure H<sub>2</sub> during the reduction. On the other hand, UV-vis spectra of both NiW11 and W/SiO<sub>2</sub> reduced at 500 °C for 1 h showed the presence of monotungstate and polytungstate species with similar intensities at 213 and 268 nm, respectively (Figure S5). This indicates the presence of highly dispersed unreduced W oxides that resist reduction during the pretreatment. Since XRD is a bulk characterization technique, one may expect the presence of partially reduced and poorly crystallized WO, with small sizes, not detected by XRD.

XAS was performed to determine the local geometry of Ni and W in NiW11, as shown in Figures S6-S10 and Table 3.

Table 3. EXAFS Fitting Parameters over a Fourier Transform Range of 2.7 to 11  ${\mathring A}^{-1}$  at the Ni K Edge and W L3 Edge

sample	XANES energy (keV)	scattering pair	CN <sup>a</sup>	R (Å) <sup>a</sup>	$\delta$ (Å) <sup>a</sup>	$\frac{\Delta E_{o}}{(eV)^{a}}$
Ni K edg	e					
$Ni/SiO_2$	8.333	Ni-Ni	10.6	2.49	0.005	5.4
NiW11	8.333	Ni-Ni	7.1	2.49	0.005	4.3
Ni K edg	e difference EXAF	S (reduced-	oxidized	)		
NiW11		Ni-O	1.9	2.05	0.002	3.4
		Ni-Ni	4.1	2.49	0.005	
		Ni-W	0.9	2.52	0.005	
W L3 edg	ge					
$W/SiO_2$	10.21	W-O	4.0	1.76	0.004	-3.7
NiW11	10.21	W-O	3.4	1.76	0.004	-0.7

 $^{a}$ CN = average coordination number, R = bond distance,  $\Delta E_{0}$  = energy shift, and  $\sigma$  = Debye–Waller factor.

Both the X-ray absorption near edge structure (XANES) and Fourier transformed extended X-ray absorption fine structure (EXAFS) spectra for the Ni K edge in NiW11 are similar to those of Ni foil (Figure S6A,B), indicating that Ni oxide in the catalyst was fully reduced. However, no Ni–W bonds were observed in this bimetallic catalyst after in situ reduction, and the oscillation of the Ni K edge for both Ni/SiO<sub>2</sub> and NiW11 are also similar (Figure S10). Since XAS is a bulk technique and measures the average local coordination of Ni atoms. If there is only a small fraction of Ni–W bonds compared to Ni–Ni bonds, in combination with a similar bond distance for Ni–Ni (2.49 Å) and Ni–W (2.55 Å) scattering pairs, it would be difficult to deconvolute the Ni–W scattering pair in the average structure.

To determine if any Ni–W bonds were present and their approximate location in the nanoparticle, difference analysis between the fully reduced nanoparticle and the oxidized nanoparticle post reduction (reduced minus oxidized) was performed at the Ni K edge to isolate the surface contribution of the nanoparticle.<sup>60</sup> This method relies on the selective

oxidation of the surface. Therefore, the difference spectrum represents only the bonds from the surface. This comparison is made in Figure 7A, which shows the reduced and oxidized FT

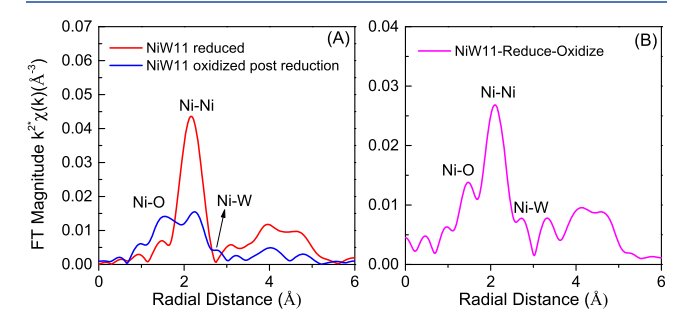


**Figure 7.** Magnitude of Fourier transform of the  $k^2$  weighted EXAFS spectra of (A) reduced at 500 °C (red) and subsequentially oxidized (blue) Ni11 catalyst and (B) reduced—oxidized difference EXAFS.

magnitudes for NiW11. The small difference observed represents a loss of metallic coordination (Ni-Ni and Ni-W) upon oxidation and formation of Ni-O bonds. Figure 7B shows the difference EXAFS (reduced minus oxidized) and indicates that there are surface Ni-Ni, Ni-W, and Ni-O scatters. In the difference fit, the oxidized catalysts are subtracted from the reduced spectrum, so the Ni-O scattering path is  $\pi$ -radians out of phase from a normal scattering pair. Since the metallic peaks that are common to both the reduced and oxidized nanoparticles are removed in the difference spectrum, the surface Ni-O and surface Ni-Ni and Ni-W are more easily resolved and analyzed. The results of the fitting are shown in Figure S9 and Table 3 and indicate that the NiW11 catalyst contains a thin NiW alloy shell (Ni-W coordination number (CN) of ~0.9) surrounding a small Ni core (with a Ni-Ni CN of 7.1).

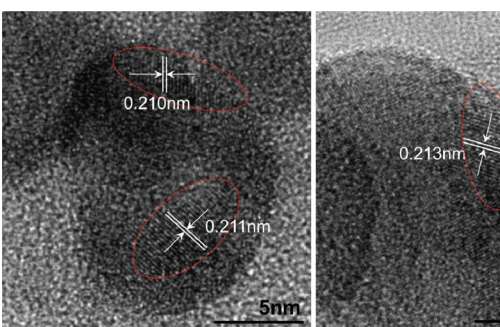
On the other hand, the XANES on the W L3 edge in NiW11 is quite similar to that of W/SiO<sub>2</sub> (Figure 6C), falling between that of W<sup>6+</sup> in NaWO<sub>4</sub> and W<sup>0</sup> in W foil (Figure S7), which indicates that the W species in both NiW11 and W/SiO<sub>2</sub> are partially reduced WO<sub>x</sub> (with 0 < x < 3). Compared to XRD results, the XANES results suggest that in addition to the crystallized W<sub>3</sub>O and NiW alloy, there must exist a fraction of poorly crystallized and/or highly dispersed WO<sub>x</sub> species, not detected by XRD.

The EXAFS at the W L3 edge (Figure S6D) shows that NiW11 and W/SiO<sub>2</sub> contain similar W–O scattering pairs with a bond distance of 1.76 Å. However, analysis of outer shells for W/SiO<sub>2</sub> gives evidence of a weak W–W scattering at 2.69 Å consistent with the W–W bond position in the W foil. Moreover, the NiW11 catalyst exhibited two scatterings at 2.48 and 2.89 Å, which are likely related to small contributions from Ni–W and W–W bonds, respectively, supporting the concept that NiW11 only contains a small fraction of the NiW alloy phase.

In summary, NiW11 contains a thin NiW alloy shell with a Ni core as well as  $WO_x$  species. Since Ni and W species strongly interact with each other as suggested by  $H_2$ -TPR, it could be proposed that the NiW11 catalyst is composed of a Ni–W alloy shell with a small Ni core and  $WO_x$  in close proximity. In addition, the radial distribution function results from DFT calculation show that the EXAFS-derived bond distances for Ni–Ni, Ni–W, and W–W of NiW11 resemble

more closely to the bulk Ni<sub>1</sub>W<sub>1</sub> alloy than the Ni<sub>4</sub>W<sub>1</sub> alloy (Figure S11).

TEM analysis was then performed to further investigate the structure of the catalysts. As TEM could observe a local environment, it helps in detecting the NiW alloy phases on reasonably large particles that cannot be detected by pristine XAS. TEM images of W/SiO<sub>2</sub> show poorly crystallized WO<sub>x</sub> species forming large aggregates, while the NiW11 sample shows nanoparticles (<10 nm) distributed on the SiO<sub>2</sub> support (Figure S12). HRTEM images of NiW11 (Figure 8) revealed



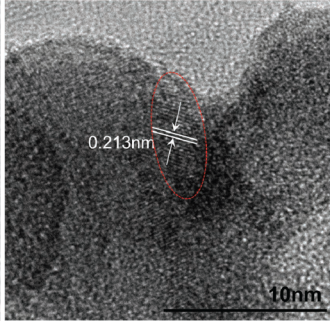


Figure 8. HRTEM images of the NiW11 catalyst, which was prereduced at 500 °C.

the presence of lattice fringes of 0.210-0.213 nm, which are in good agreement with the lattice distance (~0.210 nm) of the NiW alloy at  $2\theta = 42.99^{\circ}$  observed by XRD, suggesting the formation of the NiW alloy. Poorly crystallized WO<sub>x</sub> was found to be in close contact with the NiW alloy, while no lattice fringes of metallic Ni were found (Figure 8). Taking into account the results from XRD and EXAFS, one may expect that the core of the bimetallic particles is composed by small Ni clusters, which are not resolved by HRTEM. In addition, EDS was performed on the catalyst to further map the distribution of Ni and W species. Figure 9A,B clearly shows that Ni and W are in close proximity to each other, with W slightly more widely distributed. These results confirm the close interaction between Ni and W. Line scans were performed to reveal the distribution of Ni and W in a given particle. Figure 9C shows very similar Ni and W distributions along the scanning line but it becomes richer in Ni toward the core, suggesting the formation of the NiW alloy with a Ni core. Figure 9D also shows that W is richer on one side of the scanning line, implying WO<sub>x</sub> species are adjacent to the NiW

In parallel with the structural analysis, the electronic interaction between Ni and W was analyzed by XPS. Note that in this case the samples were reduced ex situ before XPS measurements and transferred via a glovebox into the XPS chamber to minimize exposure to air. In any case, this transfer may not completely exclude the chance of partial oxidation of the nanoparticle surface during the transfer to the instrument. An important aspect to note is that the same treatment and transfer process were followed for all samples. Thus, any observed difference must be ascribed to intrinsic structural differences in the catalyst. Figure 10A shows the Ni 2p spectra of Ni/SiO<sub>2</sub> and NiW samples. The deconvoluted peaks at  $\sim$ 852.7,  $\sim$ 855.7, and  $\sim$ 859.5 eV can be assigned to the Ni<sup>0</sup>, Ni<sup>2+</sup>, and the satellite peak of Ni<sup>2+</sup>, respectively.<sup>22,38</sup> Notably, the binding energy (BE) for Ni<sup>0</sup> in NiW gradually shifts to higher values with increasing W loadings. This shift indicates

that the electronic interaction between Ni and W lowers the d band electron density of Ni. Figure 10B shows the W 4d spectra of W/SiO<sub>2</sub> and NiW samples. Here, we used the W 4d peak instead of W 4f since the latter overlaps with that of O 2s (Figure S13). Bigey et al. reported that reduction of WO<sub>3</sub> leads to the appearance of W5+, W4+, and W0 species. 57 Since W6+ and W4+ correspond to well-defined oxides while the BE of W<sup>5+</sup> is less certain, we have deconvoluted the W 4d spectra based on the well-defined  $W^0$ ,  $W^{4+}$ , and  $W^{6+}$  BEs for  $4\bar{d}_{5/2}$  at  $\sim$ 243.3,  $\sim$ 246.2, and  $\sim$ 248.5 eV, respectively (see Figure 10B). It is evident that the BE for W<sup>0</sup> shifts to lower values with increasing W/Ni ratio. Combined with the concomitant shifts of Ni<sup>0</sup>, this result is consistent with an electron transfer from Ni to W.

The valence state distributions of Ni and W are shown in Table 4. The NiW catalysts had significantly less Ni<sup>2+</sup> than Ni/  $SiO_2$ , implying that the presence of surface  $WO_x$  in close proximity to Ni species prevents their oxidation. On the other hand, W/SiO<sub>2</sub> has a larger fraction of W<sup>6+</sup> and less W<sup>0</sup> than the NiW catalysts, indicating that the presence of Ni facilitates the reduction of the W oxide in its proximity. The surface site concentrations derived from XPS are shown in Table 4. The nominal bulk W/Ni molar ratios were 0.5, 1, and 2 for NiW21, NiW11, and NiW12, respectively. Interestingly, the surface W/ Ni molar ratios derived from XPS were significantly higher than the bulk value, indicating an enrichment of W species on the surface, which is in good agreement with TEM and XAS observations. This phenomenon could also be seen by analysis of the surface Ni concentration. NiW21 shows a higher surface Ni concentration (Ni/Si = 0.019) than Ni/SiO<sub>2</sub> (0.010). As suggested by XRD and EXAFS, this is due to the presence of W in NiW21 with improved Ni dispersion. However, further increasing the W loading results in a decreased Ni/Si ratio (0.014 for NiW11 and 0.009 for NiW12), which could be resulted from the enrichment of WO<sub>x</sub> covering the surface of

The surface structure of the NiW catalyst was further probed by CO chemisorption. Interestingly, no CO adsorption was detected on NiW11 at room temperature, indicating the absence of pure Ni surface ensembles, which are known to strongly adsorb CO. This difference can be attributed to the resulting structure of Ni, which becomes atomically isolated in the NiW surface alloy and/or covered by the surface WO<sub>x</sub> species. Furthermore, the surface Ni atoms in the NiW alloy may become electron-deficient—as indicated by the XPS results—which also result in a weakened CO-Ni interaction due to the reduced back-donation from Ni. These characteristics may explain the weak hydrogenation activity of the NiW11 catalyst.

The acidity of the catalysts was probed by NH<sub>3</sub>-TPD (Figure S14 and Table 2). While, as expected, the Ni/SiO<sub>2</sub> catalyst only displayed a weak desorption peak, centered at 100 °C, the bimetallic NiW catalysts and W/SiO<sub>2</sub> showed a stronger acidity, evidenced by a desorption peak at ~120 °C, with a tail extending up to 400 °C. The density of NH<sub>3</sub>adsorbing sites is 15.2 µmol/g<sub>cat</sub> on Ni/SiO<sub>2</sub>, which is eight times less than that on W/SiO<sub>2</sub> with the same mol of metal loadings. Increasing W loading in the bimetallic NiW catalysts led to increased density of acid sites, indicating that the NH3adsorbing sites are mainly related to the W species. Infrared spectra of pyridine adsorption at 150 °C suggested that Lewis acid sites (LASs) are the dominant acid sites in NiW samples (Figure S15). In accordance with previous studies, 61,62 the ACS Catalysis pubs.acs.org/acscatalysis Research Article

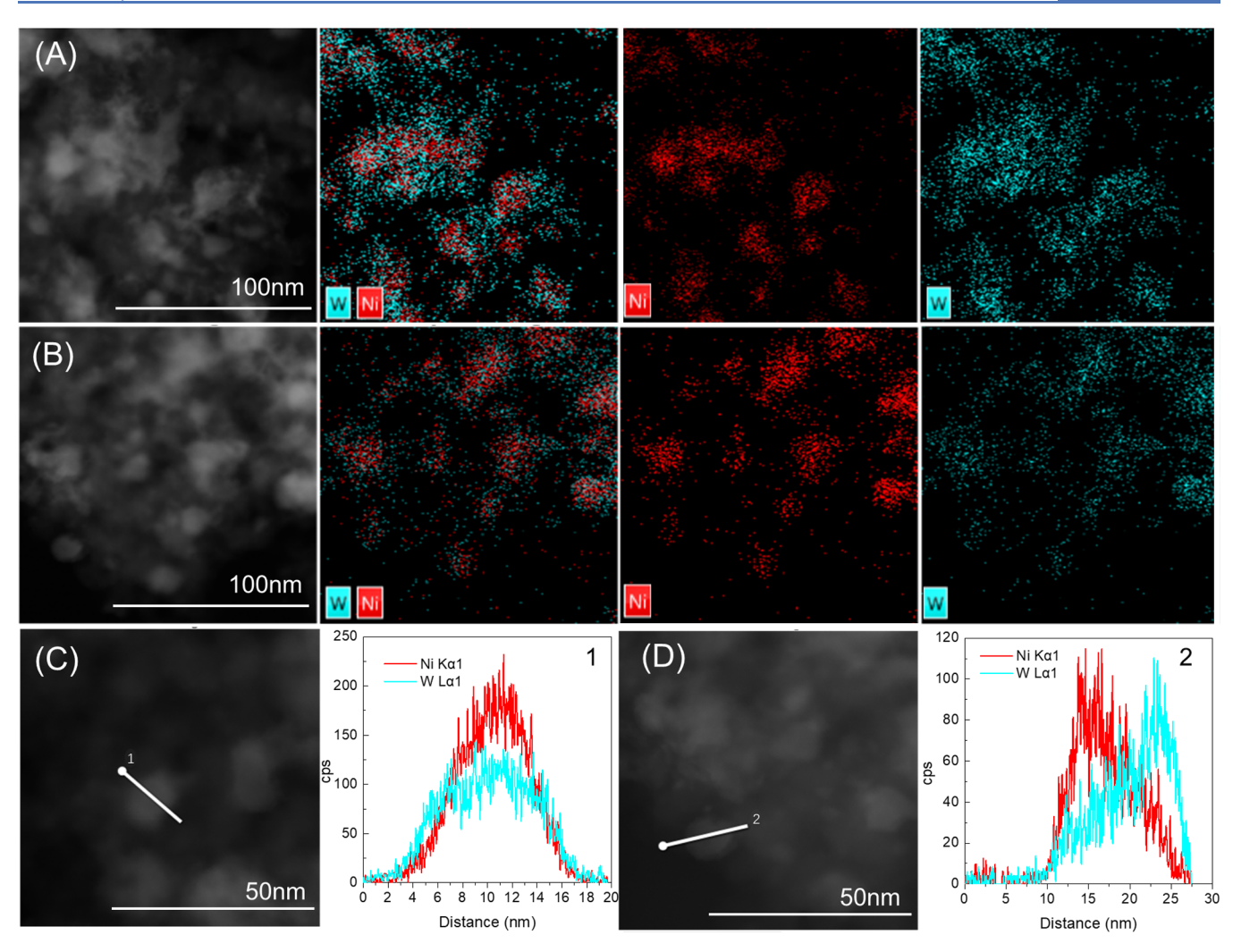
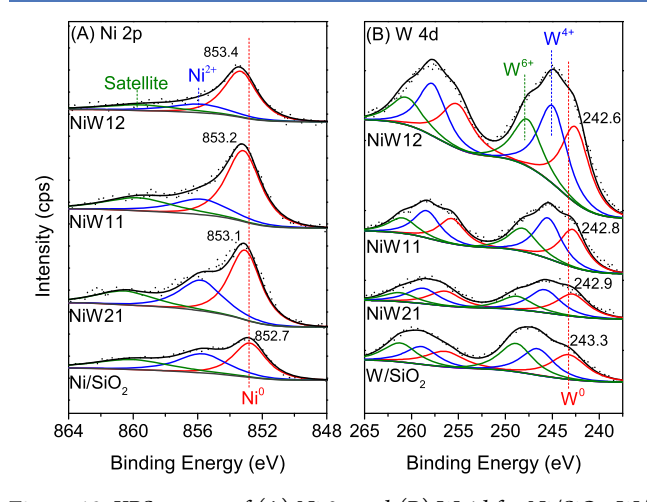


Figure 9. (A and B): HAADF-STEM images with corresponding EDS mapping of Ni and W elements; (C and D): HAADF-STEM images with line scanning for the NiW11 catalyst. The catalyst was prereduced at 500 °C.



**Figure 10.** XPS spectra of (A) Ni 2p and (B) W 4d for Ni/SiO<sub>2</sub>, W/SiO<sub>2</sub> and NiW with different W/Ni molar ratios. The catalysts were ex-situ reduced in  $H_2$  at 500 °C.

 ${
m SiO_2}$ -supported W catalysts usually show weak and little Brønsted acid sites. Note that the acid density of different catalysts can be well correlated with the observed MCHol dehydration activity (Figure S16). However, it cannot be correlated with the deoxygenation activity of m-cresol toward

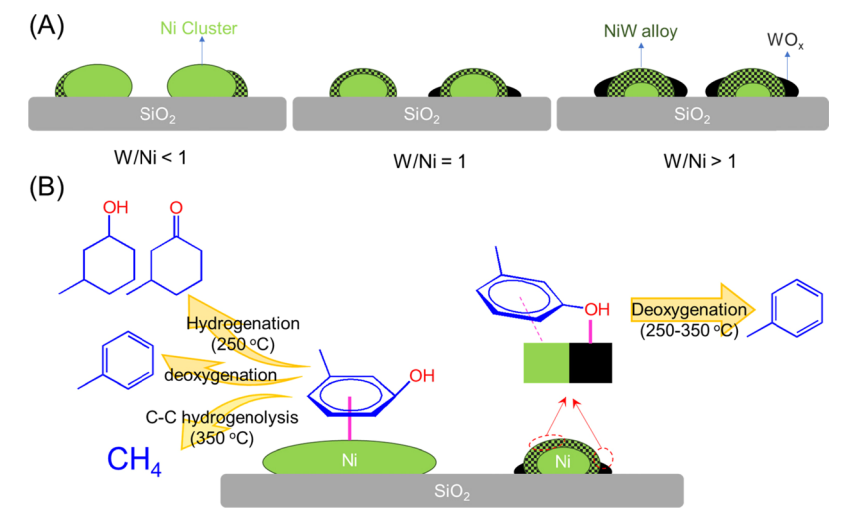
Tol (Figure S17). Clearly, bare W/SiO<sub>2</sub> has a large amount of LASs but shows extremely low deoxygenation activity. Moreover, NiW12 has much more acid sites than NiW11, while they have comparable deoxygenation activities since the extra LASs in NiW12 are away from the Ni site. It indicates that only the LAS (or coordinatively unsaturated W sites) in close proximity to Ni, that is, the Ni–W neighboring site, can play a role in deoxygenation of *m*-cresol to toluene. The LAS (coordinatively unsaturated metal cation) is oxophilic and therefore could adsorb the O atom of cresol. Similar to the Ni–Re catalyst,<sup>22</sup> the Ni–W neighboring sites on the Ni–W catalyst enable direct cleavage of the C–O bond of cresol or partially hydrogenated cresol, resulting in the formation of toluene (see below Scheme 1B).

**3.3. Discussion.** 3.3.1. Correlating the Structure of NiW Catalysts with HDO Performance. The XRD, Raman, and UV-vis characterizations clearly indicate that the extent of interaction between NiO and WO<sub>3</sub> is strongly influenced by the W/Ni ratio, with the maximum achieved on NiW11. This strong oxide—oxide interaction affects the Ni and W species interactions in reduced samples. From the combination of several characterization techniques, we propose a structure model for the reduced bimetallic NiW catalysts. As shown in Scheme 1A, the NiW11 catalyst has a NiW alloy shell surrounding a small metallic Ni cluster core, with WO<sub>x</sub> species

Table 4. Distribution of Different Valence States of Ni and W As Well as Atomic Ratios Derived from XPS

	distribution of valence states							
	N	<b>V</b> i	W		atomic ratio			
catalyst	Ni <sup>0</sup>	Ni <sup>2+</sup>	$W^0$	W <sup>4+</sup>	W <sup>6+</sup>	Ni/Si	W/Si	W/Ni
Ni/SiO <sub>2</sub>	0.55	0.45				0.010		
W/SiO <sub>2</sub>			0.33	0.32	0.35		0.016	
NiW21	0.63	0.37	0.38	0.39	0.23	0.019	0.013	0.68
NiW11	0.74	0.26	0.37	0.40	0.24	0.014	0.018	1.28
NiW12	0.76	0.24	0.38	0.39	0.23	0.009	0.053	5.36

Scheme 1. (A) Proposed Catalyst Structure after Reduction at 500 °C, which Include Metallic Ni (Green), NiW Alloy (Pattern, WO<sub>x</sub> (Black) and SiO<sub>2</sub> Support (Gray); (B) m-Cresol Adsorption and Product Distribution over the Pure Ni Sites and Ni–W/WO<sub>x</sub> Neighboring Sites, Respectively<sup>a</sup>



"On pure Ni site ensembles of Ni/SiO<sub>2</sub>, phenyl-ring hydrogenation is the major pathway at 250 °C; C–C hydrogenolysis is the dominant pathway at 350 °C; while it is unselective for the three pathways at 300 °C. In contrast, deoxygenation is the dominant pathway on Ni–W/WO<sub>x</sub> neighboring sites of NiW11 at 250–350 °C.

in its proximity. The small Ni particles detected by EXAFS cannot be located on the surface, since no CO chemisorption or typical activity of Ni is observed on this catalyst. Direct modification of the Ni nanoparticles by surface WO<sub>x</sub> without formation of the NiW alloy is unlikely either, since lattice fringes of Ni were not observed in HRTEM while those for a NiW alloy were clearly evident. Thus, it can be concluded that a small Ni core is at the center of the NiW bimetallic particles due to an incomplete formation of the NiW alloy, which is consistent with the line scanning results obtained with TEM. In this case, the covered Ni core may not directly participate in the reaction but may stabilize the NiW alloy shell. On the catalysts with W/Ni < 1, in addition to the NiW alloy, isolated larger Ni particles are formed. Finally, when W/Ni > 1, isolated WO<sub>x</sub> aggregates formed in addition to the NiW alloy. Note that the size of the Ni particle (or core) was smaller as the W content increased.

For the optimal NiW11 catalyst, the intrinsic properties of Ni were significantly suppressed by the presence of W species, which strongly interact with Ni and influence its properties. The formation of the NiW alloy (see XRD, EXAFS, and TEM results) and further modification by  $WO_x$  (see UV–vis, EXAFS, TEM, and XPS results) dilutes surface Ni ensembles, resulting in isolated surface Ni. In addition, as shown by XPS, electronic interactions with W cause a reduced density of delectrons in Ni. These geometric and electronic interactions were further confirmed by the absence of CO adsorption on

NiW11 at room temperature. Since CO adsorbs on transition metals through its C atom, one could expect a weakened adsorption of m-cresol and products (Tol, MCHane, MCHone, and others) on the NiW11 surface through C atoms. As a result, on such an active site, m-cresol may prefer to adsorb through the O atom on the more oxophilic W species (in the NiW alloy and/or WO<sub>x</sub> species in close proximity to Ni), which eventually facilitates the C-O breakage of m-cresol toward toluene, in contrast to the high tendency toward phenyl-ring hydrogenation and C-C hydrogenolysis on pure Ni site ensembles (Scheme 1B). In this case, the role of Ni should be dissociation of H2, hydrogenation of CH<sub>3</sub>C<sub>6</sub>H<sub>4</sub>\* and OH\* species, and regeneration of oxygen vacancies in WO<sub>x</sub> species. Hence, a highly efficient deoxygenation of m-cresol is achieved on NiW11, which has the balanced ability for cleaving C-O bonds and hydrogenating intermediates. On the other hand, the weakened adsorption of intermediates through C atoms may facilitate the desorption of products and reduce both, ring hydrogenation and C-C hydrogenolysis reactions. Theoretically, the C-C hydrogenolysis requires the two C atoms to lose all the H and each to form three C metal bonds before C-C cleavage in the transition state. 13,63,64 That is, at least 4-6 neighboring Ni atoms are needed for C-C hydrogenolysis. The isolated Ni sites diluted by W and/or modified by WO<sub>x</sub> is not favorable for the formation of the transition state for C-C hydrogenolysis. Thus, C-C hydrogenolysis toward CH<sub>4</sub> is completely

inhibited on NiW11 even at 350 °C. For NiW catalysts with W/Ni < 1, there were isolated larger Ni particles, which are less efficient for deoxygenation due to a lower oxophilicity of Ni to attract the O atom in m-cresol, 25,65 resulting in lowered Tol production rates. For the NiW catalysts with W/Ni > 1, excess WO $_x$  away from Ni species is formed, which has little effect on deoxygenation, resulting in minor improvement in Tol production. Compared to other Ni-based bimetallic catalysts, such as NiRe, NiFe, 3 and NiGa, 4 the optimal NiW11 shows the advantage of complete inhibition of C–C hydrogenolysis to CH $_4$  at relatively high temperatures. Clearly, this is attributed to the strong interaction between NiO and WO $_3$ , which creates small NiW alloy clusters with WO $_x$  in proximity after mild reduction (Scheme 1A).

In addition to the W/Ni ratio, other preparation parameters, such as the loading sequence and calcination/reduction temperature, can also have a strong influence in the resulting structure of the bimetallic NiW catalysts. Indeed, the XRD analysis indicates that the NiW11 catalyst, prepared by sequential impregnation resulted in larger NiO and WO3 particles than those on the catalyst prepared by coimpregnation (Figure S18A). Raman results further confirm that the sequential impregnated Ni<sup>1</sup>W<sup>2</sup>-11 and W<sup>1</sup>Ni<sup>2</sup>-11 show intense WO3 crystallite vibrations with unobservable interaction with NiO, while only the coimpregnated NiW11 exhibits the  $(Ni-O)_2-W(=O)_2$  structure (Figure S19). Clearly, the sequential impregnation results in a lower extent of interactions between NiO and WO3. After reduction, larger Ni and W<sub>3</sub>O particles were obtained over Ni<sup>1</sup>W<sup>2</sup>-11 and  $W^1Ni^2-11$  (Figure S18B), which eventually led to lower mcresol conversion and toluene yield (Table 1). In addition, XPS analysis has demonstrated that the impregnation sequence influences the relative surface concentrations of Ni and W species, that is, the second loaded metal had a higher surface concentration (Figure S20 and Table S4). However, neither loading Ni first nor W first-with more W or Ni on the surface, respectively—resulted in activity or selectivity as high as those obtained when the metals were loaded simultaneously, by coimpregnation (Table 1). This indicates that a balance between surface Ni and W species is essential to achieve the best HDO performance.

The calcination/reduction temperature also affects the HDO performance. Previous work has shown that formation of NiMoO<sub>4</sub> during calcination leads to the structure with the highest HDO activity/selectivity of the Ni-Mo catalyst after reduction.<sup>28</sup> Here, however, increasing the calcination temperature to 750 °C led to the formation of NiWO<sub>4</sub> in the sample NiW11-750 (Figure S18A). Nevertheless, after reduction at 500 °C, this sample showed similar HDO activity and activation energy for Tol formation as that when calcined at 500 °C (Figures S1 and S21), which had no appreciable amounts of NiWO<sub>4</sub>. In fact, XPS confirmed that the two reduced samples had similar surface composition and valence states (Figure S22 and Table S4). Moreover, XRD indicated that part of the NiWO<sub>4</sub> precursor remained unreduced (Figure S18B). However, the increase in the reduction temperature of NiW11-750 to 600 °C sharply decreased the HDO activity (Figure S23), possibly due to the sintering of the active phase. This comparison indicates that the formation of NiWO<sub>4</sub> is not necessary for the formation of the active site for efficient HDO, as it was the case for Ni-Mo catalysts. Moreover, increasing the reduction temperature to 600 °C for NiW11 (calcined at 500 °C) also caused a decrease in activity (Figure S1B), as

higher reduction temperature led to the disappearance of the NiW alloy phase and formation of the larger Ni and W particles, as shown in XRD (Figure S24). Again, these results highlight the importance of the formation of the NiW alloy with adjacent WO, for efficient HDO.

3.3.2. Comparison of NiW, NiMo, and NiRe Bimetallic Catalysts. Previous work has shown that addition of either Mo or Re can improve the direct deoxygenation to Tol on Nibased catalysts while inhibiting C-C hydrogenolysis to CH<sub>4</sub>. <sup>22,28</sup> Since W is in the same group and period as Mo and Re, it is interesting to compare their structure and performance in HDO. For the bimetallic catalysts calcined under mild conditions (400-500 °C), NiMo formed a solid solution of NiMoO<sub>4</sub>, while NiW and NiRe catalysts formed  $(-O)_2$ -W(=O)<sub>2</sub> and -O-Re(=O)<sub>3</sub> species attached to the NiO surface, respectively.<sup>22</sup> This could be due to the similarity of the atomic diameters of Ni and Mo, which results in a high mutual solubility of NiO and MoO<sub>3</sub>. By contrast, the much larger diameters of W and Re compared to Ni result in lower solubilities with NiO; thus, higher calcination temperatures are needed to form solid solutions with NiO (see Figure S18A). After reduction at intermediate temperatures (450-500 °C), different structures resulted for the bimetallic catalysts. The NiMo catalysts formed a Ni core, with MoOx species segregated to the Ni surface. While NiW and NiRe catalysts formed bimetallic alloys with a Ni core and  $MeO_x$  (Me = Mo and Re) in their proximity, it appeared that the NiW catalyst displayed a higher extent of alloying than NiRe.

The calculated oxygen and hydrogen adsorption energies for W, Mo, Re, and Ni surfaces are compared in Table 5 and

Table 5. DFT-Calculated Adsorption Energies of Atomic O and H on Different Metal Surfaces

metal surface	E(O)/eV	E(H)/eV
Ni(111)	-2.36	-0.54
Re(0001)	-3.63	-0.68
Mo(110)	-4.18	-0.82
W(110)	-4.38	-0.88

Figure S25. W and Mo have similar oxophilicities, which are higher than that of Re and much higher than Ni. This trend is consistent with the reducibility of these metal oxides measured by  $H_2$ -TPR, i.e., Ni > Re > Mo > W. Also, W and Mo display stronger binding to H than Re and much stronger than Ni; this is consistent with the well-known hydrogenation activity of Ni, while on the others H is irreversibly chemisorbed. The extent of alloy formation is also related to the reducibility of the corresponding oxides and phase stability of the intermediate MeO<sub>x</sub> during reduction. Although Mo is slightly less oxophilic than W, Mo does not form alloys with Ni while W does. This is expected from the high stability of the intermediate MoO<sub>2</sub> (Figure S26), 66 compared to the less stable intermediate oxide for W (Figure S27). 67 Indeed, the H2-TPR results showed that MoO<sub>3</sub> exhibits multiple reduction peaks in a wide reduction region, while WO<sub>3</sub> showed one overlapping reduction peak. Therefore, MoO3 tends to be reduced to MoO2 such as MoO<sub>2</sub>, under mild reduction conditions, <sup>28</sup> while WO<sub>3</sub> tends to be reduced to W<sub>3</sub>O or even metallic W (see XRD and H<sub>2</sub>-TPR results). As a result, reduced W forms alloys with Ni in proximity, while MoO<sub>x</sub> does not but decorates the surface of Ni. Similarly, reduced Re can also form NiRe alloys but to a less extent than W, which is likely due to the larger diameter of Re than W and therefore slower diffusion of Re in Ni to form an alloy.<sup>68</sup>

Both NiW11 and NiMo11 catalysts completely inhibit C-C hydrogenolysis to CH4 and improve deoxygenation to Tol at 350 °C, which is clearly related to their high oxophilicity (Table 5). However, the NiW11 catalyst is ~2.5 times more active than NiMo11 (Table S5). This is probably due to the two different core-shell structures. The Ni surface in the NiMo11 catalyst is decorated by MoO<sub>x</sub> species which hinder the accessibility of Ni to both H2 and the reactant. By contrast, the Ni core surface of NiW11 is a NiW alloy in which the surface Ni atoms are still accessible to H2 but their affinity to the C atom is significantly weakened. As a result, the hydrogenation ability of NiMo11 is lower than that of NiW11, leading to lowered deoxygenation activity. Indeed, the lowered hydrogenation ability is supported by the distribution of minor products of MCHene and MCHane at 250 °C. As shown in Figure S28, NiW11 showed mainly MCHane while NiMo11 showed mainly MCHene.

Finally, the NiRe bimetallic catalyst, while it also forms surface NiRe alloys, behaves somewhat differently from NiW11 and NiMo11. Unlike NiW11 and NiMo11, the optimal NiRe catalyst cannot completely inhibit C-C hydrogenolysis, while it retains hydrogenation reactions at low conversions (Table S5). Moreover, NiRe can still adsorb CO at room temperature, indicating a stronger adsorption of the reactant through its C atoms. These results are consistent with Re being much less oxophilic than W or Mo (Table 5), which may result in less modification of the intrinsic properties of the adjacent Ni atoms. Furthermore, the hydrogenation ability of Re is closer to that of Ni than those of W and Mo (Table 5), which explains the hydrogenation activity of the NiRe catalyst (Table S5). As a result, the optimal NiRe catalyst is more active than NiMo and NiW for m-cresol conversion under identical mild reaction conditions (Table S5).

# 4. CONCLUSIONS

A bimetallic NiW/SiO<sub>2</sub> catalyst, prepared by coimpregnation with a W/Ni molar ratio of 1, shows about an order of magnitude higher activity than monometallic Ni/SiO2 for HDO of *m*-cresol at 350 °C and 1 atm H<sub>2</sub>. More importantly, it avoids two side reactions that would typically lower selectivity: C-C hydrogenolysis to CH<sub>4</sub> at 350 °C and the ring hydrogenation reaction at 250 °C. Various characterization techniques were employed to elucidate the structure of this efficient NiW/SiO2 catalyst. The calcined NiW/SiO2 gave evidence for a strong Ni and W oxide interaction involving a  $(Ni-O)_2-W(=O)_2$  structure. After reduction at 500 °C, a complex structure is formed, composed of a thin NiW alloy shell surrounding a small Ni core, with WO<sub>x</sub> in close proximity. Furthermore, an electronic interaction between Ni and W is evidenced by both XANES and XPS. This interaction alters the intrinsic properties of Ni, resulting in significantly weakened CO chemisorption and unique catalytic properties. The activity of this catalyst for hydrogenation and C-O cleavage is well balanced, providing improved activity toward toluene with inhibition of undesirable CH<sub>4</sub> and ring-hydrogenation product formation. The optimal NiW bimetallic catalyst is more selective and more active than previously reported NiRe and NiMo catalysts, respectively.

#### ASSOCIATED CONTENT

# **Supporting Information**

The Supporting Information is available free of charge at https://pubs.acs.org/doi/10.1021/acscatal.0c05560.

Effect of the preparation method, calcination/reduction temperature of NiW11 on the structure (characterized by XRD, Raman, and XPS) and HDO performance, product distributions at 350 and 250 °C, 3-methycyclohexanol dehydration, XPS spectra of W 4d, UV-vis of reduced NiW11 and W/SiO2, XANES and EXAFS spectra of Ni K edge and W L3 edge for reduced samples, radial distribution functions of bulk Ni<sub>4</sub>W<sub>1</sub> and Ni<sub>1</sub>W<sub>1</sub> alloys, TEM image of different samples, NH<sub>3</sub>-TPD, the relationship between LASs with dehydration activity and deoxygenation activity, and apparent activation energy over NiW11-750, DFT calculation for O and H adsorption over Ni, Re, Mo, and W metal surfaces, phase diagram of Mo-O and W-O systems, comparison of MCHene and MCHane yields as a function of m-cresol conversion over NiMo11 and NiW11, and comparison of *m*-cresol conversion over Ni, NiRe, NiMo, and NiW (PDF).

## AUTHOR INFORMATION

## **Corresponding Authors**

Xinli Zhu — Collaborative Innovation Center of Chemical Science and Engineering, School of Chemical Engineering and Technology, Tianjin University, Tianjin 300072, China; Email: xinlizhu@tju.edu.cn

Daniel E. Resasco — School of Chemical, Biological, and Materials Engineering, The University of Oklahoma, Norman, Oklahoma 73019, United States; oorcid.org/0000-0001-5342-0621; Email: resasco@ou.edu

# **Authors**

Feifei Yang — Collaborative Innovation Center of Chemical Science and Engineering, School of Chemical Engineering and Technology, Tianjin University, Tianjin 300072, China; School of Chemical, Biological, and Materials Engineering, The University of Oklahoma, Norman, Oklahoma 73019, United States

Mallikharjuna Rao Komarneni – School of Chemical, Biological, and Materials Engineering, The University of Oklahoma, Norman, Oklahoma 73019, United States

Nicole J. Libretto – Davidson School of Chemical Engineering, Purdue University, West Lafayette, Indiana 47907, United States

 Liwen Li – Collaborative Innovation Center of Chemical Science and Engineering, School of Chemical Engineering and Technology, Tianjin University, Tianjin 300072, China

Wei Zhou — Collaborative Innovation Center of Chemical Science and Engineering, School of Chemical Engineering and Technology, Tianjin University, Tianjin 300072, China

Jeffrey T. Miller – Davidson School of Chemical Engineering, Purdue University, West Lafayette, Indiana 47907, United States; orcid.org/0000-0002-6269-0620

Qingfeng Ge — Department of Chemistry and Biochemistry, Southern Illinois University, Carbondale, Illinois 62901, United States; o orcid.org/0000-0001-6026-6693

Complete contact information is available at: https://pubs.acs.org/10.1021/acscatal.0c05560

#### Notes

The authors declare no competing financial interest.

#### ACKNOWLEDGMENTS

This research was funded by the National Natural Science Foundation of China (21676194 and 21873067), and the U.S Department of Energy, Office of Science, Basic Energy Sciences under Award Number DE-SC0018284. Use of Advanced Photon Source was supported by the U.S. Department of Energy. MRCAT operation, beamline 10-BM are supported by the Department of Energy and the MRCAT member institutions. N.J.L. and J.T.M. were supported in part by the National Science Foundation under Cooperative Agreement No. EEC-1647722, and National Science Foundation, Chemical, Engineering, Biological, and Transport Systems (CBET) division, award 1804712.

## REFERENCES

- (1) Vispute, T. P.; Zhang, H.; Sanna, A.; Xiao, R.; Huber, G. W. Renewable chemical commodity feedstocks from integrated catalytic processing of pyrolysis oils. *Science* **2010**, 330, 1222–1227.
- (2) Zakzeski, J.; Bruijnincx, P. C. A.; Jongerius, A. L.; Weckhuysen, B. M. The Catalytic Valorization of Lignin for the Production of Renewable Chemicals. *Chem. Rev.* **2010**, *110*, 3552–3599.
- (3) Bridgwater, A. V. Review of fast pyrolysis of biomass and product upgrading. *Biomass Bioenergy* **2012**, *38*, 68–94.
- (4) Hicks, J. C. Advances in C-O Bond Transformations in Lignin-Derived Compounds for Biofuels Production. *J. Phys. Chem. Lett.* **2011**, *2*, 2280–2287.
- (5) Saidi, M.; Samimi, F.; Karimipourfard, D.; Nimmanwudipong, T.; Gates, B. C.; Rahimpour, M. R. Upgrading of lignin-derived biooils by catalytic hydrodeoxygenation. *Energy Environ. Sci.* **2014**, *7*, 103–129.
- (6) Bu, Q.; Lei, H.; Zacher, A. H.; Wang, L.; Ren, S.; Liang, J.; Wei, Y.; Liu, Y.; Tang, J.; Zhang, Q.; Ruan, R. A review of catalytic hydrodeoxygenation of lignin-derived phenols from biomass pyrolysis. *Bioresour. Technol.* **2012**, *124*, 470–477.
- (7) Mortensen, P. M.; Gardini, D.; de Carvalho, H. W. P.; Damsgaard, C. D.; Grunwaldt, J. D.; Jensen, P. A.; Wagner, J. B.; Jensen, A. D. Stability and resistance of nickel catalysts for hydrodeoxygenation: carbon deposition and effects of sulfur, potassium, and chlorine in the feed. *Catal. Sci. Technol.* **2014**, *4*, 3672–3686
- (8) Zhao, C.; Kasakov, S.; He, J.; Lercher, J. A. Comparison of kinetics, activity and stability of Ni/HZSM-5 and Ni/Al<sub>2</sub>O<sub>3</sub>-HZSM-5 for phenol hydrodeoxygenation. *J. Catal.* **2012**, *296*, 12–23.
- (9) Mortensen, P. M.; Grunwaldt, J. D.; Jensen, P. A.; Jensen, A. D. Screening of Catalysts for Hydrodeoxygenation of Phenol as a Model Compound for Bio-oil. *ACS Catal.* **2013**, *3*, 1774–1785.
- (10) Zhao, C.; Kou, Y.; Lemonidou, A. A.; Li, X.; Lercher, J. A. Highly selective catalytic conversion of phenolic bio-oil to alkanes. *Angew Chem. Int. Ed. Engl.* **2009**, *48*, 3987–3990.
- (11) Shao, Y.; Xia, Q.; Dong, L.; Liu, X.; Han, X.; Parker, S. F.; Cheng, Y.; Daemen, L. L.; Ramirez-Cuesta, A. J.; Yang, S.; Wang, Y. Selective production of arenes via direct lignin upgrading over a niobium-based catalyst. *Nat. Commun.* **2017**, *8*, 16104.
- (12) Pourzolfaghar, H.; Abnisa, F.; Wan Daud, W. M. A.; Aroua, M. K. Atmospheric hydrodeoxygenation of bio-oil oxygenated model compounds: A review. *J. Anal. Appl. Pyrol.* **2018**, *133*, 117–127.
- (13) Yang, F.; Liu, D.; Zhao, Y.; Wang, H.; Han, J.; Ge, Q.; Zhu, X. Size Dependence of Vapor Phase Hydrodeoxygenation of m-Cresol on Ni/SiO<sub>2</sub> Catalysts. ACS Catal. **2018**, *8*, 1672–1682.
- (14) Prasomsri, T.; Shetty, M.; Murugappan, K.; Román-Leshkov, Y. Insights into the catalytic activity and surface modification of MoO<sub>3</sub> during the hydrodeoxygenation of lignin-derived model compounds into aromatic hydrocarbons under low hydrogen pressures. *Energy Environ. Sci.* **2014**, *7*, 2660–2669.

- (15) Zhu, X.; Lobban, L. L.; Mallinson, R. G.; Resasco, D. E. Bifunctional transalkylation and hydrodeoxygenation of anisole over a Pt/HBeta catalyst. *J. Catal.* **2011**, *281*, 21–29.
- (16) Moon, J. S.; Kim, E. G.; Lee, Y. K. Active sites of Ni<sub>2</sub>P/SiO<sub>2</sub> catalyst for hydrodeoxygenation of guaiacol: A joint XAFS and DFT study. *J. Catal.* **2014**, *311*, 144–152.
- (17) Chen, C.; Chen, G.; Yang, F.; Wang, H.; Han, J.; Ge, Q.; Zhu, X. Vapor phase hydrodeoxygenation and hydrogenation of m-cresol on silica supported Ni, Pd and Pt catalysts. *Chem. Eng. Sci.* **2015**, *135*, 145–154.
- (18) Liu, D.; Li, G.; Yang, F.; Wang, H.; Han, J.; Zhu, X.; Ge, Q. Competition and Cooperation of Hydrogenation and Deoxygenation Reactions during Hydrodeoxygenation of Phenol on Pt(111). *J. Phys. Chem. C* 2017, 121, 12249–12260.
- (19) Robinson, A. M.; Hensley, J. E.; Medlin, J. W. Bifunctional Catalysts for Upgrading of Biomass-Derived Oxygenates: A Review. *ACS Catal.* **2016**, *6*, 5026–5043.
- (20) Hong, Y.; Zhang, H.; Sun, J.; Ayman, K. M.; Hensley, A. J. R.; Gu, M.; Engelhard, M. H.; McEwen, J. S.; Wang, Y. Synergistic Catalysis between Pd and Fe in Gas Phase Hydrodeoxygenation of m-Cresol. *ACS Catal.* **2014**, *4*, 3335–3345.
- (21) Robinson, A.; Ferguson, G. A.; Gallagher, J. R.; Cheah, S.; Beckham, G. T.; Schaidle, J. A.; Hensley, J. E.; Medlin, J. W. Enhanced Hydrodeoxygenation ofm-Cresol over Bimetallic Pt-Mo Catalysts through an Oxophilic Metal-Induced Tautomerization Pathway. ACS Catal. 2016, 6, 4356–4368.
- (22) Yang, F.; Liu, D.; Wang, H.; Liu, X.; Han, J.; Ge, Q.; Zhu, X. Geometric and electronic effects of bimetallic Ni–Re catalysts for selective deoxygenation of m-cresol to toluene. *J. Catal.* **2017**, 349, 84–97.
- (23) Nie, L.; de Souza, P. M.; Noronha, F. B.; An, W.; Sooknoi, T.; Resasco, D. E. Selective conversion of m-cresol to toluene over bimetallic Ni–Fe catalysts. *J. Mol. Catal. A: Chem.* **2014**, *388-389*, 47–55.
- (24) Zheng, Y.; Zhao, N.; Chen, J. Enhanced direct deoxygenation of anisole to benzene on SiO<sub>2</sub>-supported Ni-Ga alloy and intermetallic compound. *Appl. Catal. B: Environ.* **2019**, *250*, 280–291.
- (25) Zhou, J.; An, W.; Wang, Z.; Jia, X. Hydrodeoxygenation of phenol over Ni-based bimetallic single-atom surface alloys: mechanism, kinetics and descriptor. *Catal. Sci. Technol.* **2019**, *9*, 4314.
- (26) de Souza, P. M.; Rabelo-Neto, R. C.; Borges, L. E. P.; Jacobs, G.; Davis, B. H.; Sooknoi, T.; Resasco, D. E.; Noronha, F. B. Role of Keto Intermediates in the Hydrodeoxygenation of Phenol over Pd on Oxophilic Supports. *ACS Catal.* **2015**, *5*, 1318–1329.
- (27) Nelson, R. C.; Baek, B.; Ruiz, P.; Goundie, B.; Brooks, A.; Wheeler, M. C.; Frederick, B. G.; Grabow, L. C.; Austin, R. N. Experimental and Theoretical Insights into the Hydrogen-Efficient Direct Hydrodeoxygenation Mechanism of Phenol over Ru/TiO<sub>2</sub>. *ACS Catal.* **2015**, *5*, 6509–6523.
- (28) Yang, F.; Libretto, N. J.; Komarneni, M. R.; Zhou, W.; Miller, J. T.; Zhu, X.; Resasco, D. E. Enhancement of m-Cresol Hydrodeoxygenation Selectivity on Ni Catalysts by Surface Decoration of MoO<sub>x</sub> Species. *ACS Catal.* **2019**, *9*, 7791–7800.
- (29) Tran, N. T. T.; Uemura, Y.; Chowdhury, S.; Ramli, A. Vaporphase hydrodeoxygenation of guaiacol on Al-MCM-41 supported Ni and Co catalysts. *Appl. Catal. A: Gen.* **2016**, *512*, 93–100.
- (30) Wang, C.; Mironenko, A. V.; Raizada, A.; Chen, T.; Mao, X.; Padmanabhan, A.; Vlachos, D. G.; Gorte, R. J.; Vohs, J. M. Mechanistic Study of the Direct Hydrodeoxygenation of m-Cresol over WO<sub>x</sub>-Decorated Pt/C Catalysts. *ACS Catal.* **2018**, *8*, 7749–7759.
- (31) Hong, Y. K.; Lee, D. W.; Eom, H. J.; Lee, K. Y. The catalytic activity of  $Pd/WO_x/\gamma$ - $Al_2O_3$  for hydrodeoxygenation of guaiacol. *Appl. Catal. B: Environ.* **2014**, *150-151*, 438–445.
- (32) Meng, Q.; Yan, J.; Liu, H.; Chen, C.; Li, S.; Shen, X.; Song, J.; Zheng, L.; Han, B. Self supported hydrogenolysis of aromatic ethers to arenes. *Sci. Adv.* **2019**, *5*, No. eaax6839.
- (33) Huang, Y. B.; Yan, L.; Chen, M. Y.; Guo, Q. X.; Fu, Y. Selective hydrogenolysis of phenols and phenyl ethers to arenes through direct

- C-O cleavage over ruthenium-tungsten bifunctional catalysts. *Green Chem.* **2015**, *17*, 3010–3017.
- (34) Dwiatmoko, A. A.; Kim, I.; Zhou, L.; Choi, J. W.; Suh, D. J.; Jae, J.; Ha, J. M. Hydrodeoxygenation of guaiacol on tungstated zirconia supported Ru catalysts. *Appl. Catal. A: Gen.* **2017**, *543*, 10–16.
- (35) Ji, J.; Guo, H.; Li, C.; Qi, Z.; Zhang, B.; Dai, T.; Jiang, M.; Ren, C.; Wang, A.; Zhang, T. Tungsten-Based Bimetallic Catalysts for Selective Cleavage of Lignin C-O Bonds. *ChemCatChem* **2018**, *10*, 415–421
- (36) Jiang, G.; Hu, Y.; Xu, G.; Mu, X.; Liu, H. Controlled Hydrodeoxygenation of Phenolic Components in Pyrolysis Bio-oil to Arenes. ACS Sustainable Chem. Eng. 2018, 6, 5772–5783.
- (37) Hsu, P. J.; Jiang, J. W.; Lin, Y. C. Does a Strong Oxophilic Promoter Enhance Direct Deoxygenation? A Study of NiFe, NiMo, and NiW Catalysts in p-Cresol Conversion. ACS Sustainable Chem. Eng. 2017, 6, 660–667.
- (38) Echeandia, S.; Arias, P. L.; Barrio, V. L.; Pawelec, B.; Fierro, J. L. G. Synergy effect in the HDO of phenol over Ni–W catalysts supported on active carbon: Effect of tungsten precursors. *Appl. Catal. B: Environ.* **2010**, *101*, 1–12.
- (39) Hita, I.; Cordero-Lanzac, T.; García-Mateos, F. J.; Azkoiti, M. J.; Rodríguez-Mirasol, J.; Cordero, T.; Bilbao, J. Enhanced production of phenolics and aromatics from raw bio-oil using HZSM-5 zeolite additives for PtPd/C and NiW/C catalysts. *Appl. Catal. B: Environ.* **2019**, 259, No. 118112.
- (40) Bui, V. N.; Laurenti, D.; Afanasiev, P.; Geantet, C. Hydrodeoxygenation of guaiacol with CoMo catalysts. Part I: Promoting effect of cobalt on HDO selectivity and activity. *Appl. Catal B: Environ.* **2011**, *101*, 239–245.
- (41) Runnebaum, R. C.; Nimmanwudipong, T.; Block, D. E.; Gates, B. C. Catalytic conversion of compounds representative of ligninderived bio-oils: a reaction network for guaiacol, anisole, 4methylanisole, and cyclohexanone conversion catalysed by  $Pt/\gamma$ -Al<sub>2</sub>O<sub>3</sub>. Catal. Sci. Technol. **2012**, *2*, 113–118.
- (42) Nie, L.; Peng, B.; Zhu, X. Vapor-Phase Hydrodeoxygenation of Guaiacol to Aromatics over Pt/HBeta: Identification of the Role of Acid Sites and Metal Sites on the Reaction Pathway. *ChemCatChem* **2018**. *10*. 1064–1074.
- (43) Kresse, G.; Furthmuller, J. Efficient iterative schemes for ab initio total-energy calculations using a plane-wave basis set. *Phys. Rev. B* **1996**, *54*, 11169–11186.
- (44) Kresse, G.; Furthmüller, J. Efficiency of ab-initio total energy calculations for metals and semiconductors using a plane-wave basis set. *Comp. Mater. Sci.* **1996**, *6*, 15–50.
- (45) Blöchl, P. E. Projector augmented-wave method. *Phys. Rev. B* **1994**, *50*, 17953–17979.
- (46) Perdew, J. P.; Chevary, J. A.; Vosko, S. H.; Jackson, K. A.; Pederson, M. R.; Singh, D. J.; Fiolhais, C. Atoms, molecules, solids, and surfaces: Applications of the generalized gradient approximation for exchange and correlation. *Phys. Rev. B* **1992**, *46*, 6671–6687.
- (47) Solsona, B.; López Nieto, J. M.; Concepción, P.; Dejoz, A.; Ivars, F.; Vázquez, M. I. Oxidative dehydrogenation of ethane over Ni–W–O mixed metal oxide catalysts. *J. Catal.* **2011**, *280*, 28–39.
- (48) Aminzadeh, A.; Sarikhani-fard, H. Raman spectroscopic study of Ni/Al<sub>2</sub>O<sub>3</sub> catalyst. *Spectrochim. Acta A* **1999**, *55*, 1421–1425.
- (49) Lee, E. L.; Wachs, I. E. In Situ Spectroscopic Investigation of the Molecular and Electronic Structures of SiO<sub>2</sub> Supported Surface Metal Oxides. *J. Phys. Chem. C* **2007**, *111*, 14410–14425.
- (50) Ross-Medgaarden, E. I.; Wachs, I. E. Structure determination of bulk and surface W oxides with UV-vis diffuse reflectance spectroscopy and Raman Spectroscopy. *J. Phys. Chem. C* **2007**, *111*, 15089–15099.
- (51) liu, Z.; Chen, Y. Spectroscopic studies on tetragonal ZrO<sub>2</sub> supported MoO<sub>3</sub> and NiO-MoO<sub>3</sub> systems. *J. Catal.* **1998**, 177, 314–324.
- (52) Al Boukhari, J.; Khalaf, A.; Sayed Hassan, R.; Awad, R. Structural, optical and magnetic properties of pure and rare earth-

- doped NiO nanoparticles. Appl. Phys. A: Mater. Sci. Process. 2020, 126, 323.
- (53) Aslani, A.; Oroojpour, V.; Fallahi, M. Sonochemical synthesis, size controlling and gas sensing properties of NiO nanoparticles. *Appl. Surf. Sci.* **2011**, *257*, 4056–4061.
- (54) Maheswari, R.; Pachamuthu, M. P.; Ramanathan, A.; Subramaniam, B. Synthesis, Characterization, and Epoxidation Activity of Tungsten-Incorporated SBA-16 (W-SBA-16). *Ind. Eng. Chem. Res.* **2014**, *53*, 18833–18839.
- (55) Khatri, A.; Rana, P. S. Visible light assisted photocatalysis of Methylene Blue and Rose Bengal dyes by iron doped NiO nanoparticles prepared via chemical co-precipitation. *Phys. B* **2020**, 579, 411905.
- (56) Al Boukhari, J.; Zeidan, L.; Khalaf, A.; Awad, R. Synthesis, characterization, optical and magnetic properties of pure and Mn, Fe and Zn doped NiO nanoparticles. *Chem. Phys.* **2019**, *516*, 116–124.
- (57) Bigey, C.; Hilaire, L.; Maire, G. Catalysis on  $Pd/WO_3$  and  $Pd/WO_2$  Effect of the modifications of the surface states due to redox treatments on the skeletal rearrangement of hydrocarbons. *J. Catal.* **1999**, 184, 406–420.
- (58) Mortensen, P. M.; Grunwaldt, J. D.; Jensen, P. A.; Jensen, A. D. Influence on nickel particle size on the hydrodeoxygenation of phenol over Ni/SiO<sub>2</sub>. *Catal. Today* **2016**, *259*, 277–284.
- (59) Xiao, Z.; Zhang, Q.; Chen, T.; Wang, X.; Fan, Y.; Ge, Q.; Zhai, R.; Sun, R.; Ji, J.; Mao, J. Heterobimetallic catalysis for lignocellulose to ethylene glycol on nickel-tungsten catalysts: Influenced by hydroxy groups. *Fuel* **2018**, 230, 332–343.
- (60) Wu, Z.; Bukowski, B. C.; Li, Z.; Milligan, C.; Zhou, L.; Ma, T.; Wu, Y.; Ren, Y.; Ribeiro, F. H.; Delgass, W. N.; Greeley, J.; Zhang, G.; Miller, J. T. Changes in Catalytic and Adsorptive Properties of 2 nm Pt<sub>3</sub>Mn Nanoparticles by Subsurface Atoms. *J. Am. Chem. Soc.* **2018**, 140, 14870–14877.
- (61) Maksasithorn, S.; Debecker, D. P.; Praserthdam, P.; Panpranot, J.; Suriye, K.; Ayudhya, S. K. N. NaOH modified  $WO_3/SiO_2$  catalysts for propylene production from 2-butene and ethylene metathesis. *Chin. J. Catal.* **2014**, 35, 232–241.
- (62) Zaki, M. I.; Mekhemer, G. A. H.; Fouad, N. E.; Rabee, A. I. M. Structure—acidity correlation of supported tungsten(VI)-oxo-species: FT-IR and TPD studies of adsorbed pyridine and catalytic decomposition of 2-propanol. *Appl. Surf. Sci.* **2014**, *308*, 380–387.
- (63) Hibbitts, D. D.; Flaherty, D. W.; Iglesia, E. Role of Branching on the Rate and Mechanism of C–C Cleavage in Alkanes on Metal Surfaces. *ACS Catal.* **2015**, *6*, 469–482.
- (64) Zhao, Z. J.; Moskaleva, L. V.; Rösch, N. Tuning the selectivity for ring-opening reactions of methylcyclopentane over Pt catalysts: A mechanistic study from first-principles calculations. *J. Catal.* **2012**, 285, 124–133.
- (65) Teles, C. A.; Rabelo Neto, R. C.; de Lima, J. R.; Mattos, L. V.; Resasco, D. E.; Noronha, F. B. The Effect of Metal Type on Hydrodeoxygenation of Phenol Over Silica Supported Catalysts. *Catal. Lett.* **2016**, *146*, 1848–1857.
- (66) Zhang, C.; Gao, M. C.; Yang, Y.; Zhang, F. Thermodynamic modeling and first-principles calculations of the Mo–O system. *Calphad* **2014**, *45*, 178–187.
- (67) Wriedt, H. A. The O-W (Oxygen-Tungstem) System. Bull. of Alloy Phase Diag. 1989, 10, 368-384.
- (68) Wu, Q.; Suo, L. S.; Yue, M.; Kai, G. S. First principles calculations of alloying element diffusion coefficients in Ni using the five frequency model. *Chin. Phys. B* **2012**, *21*, 19102.